Silicon photonic integrated circuit for fast and precise dual-comb distance metrology

C. WEIMANN,[1,2,3,*] M. LAUERMANN,[1,2] F. HOELLER,[3] W. FREUDE,[1,2] AND C. KOOS[1,2,4]

[1]*Institute of Photonics and Quantum Electronics (IPQ), Karlsruhe Institute of Technology (KIT), 76131 Karlsruhe, Germany*
[2]*Institute of Microstructure Technology (IMT), KIT, 76344 Eggenstein-Leopoldshafen, Germany*
[3]*Corporate Research and Technology, Carl Zeiss AG, Oberkochen, Germany*
[4]*christian.koos@kit.edu*
[*]*claudius.weimann@zeiss.com*

Abstract: We demonstrate an optical distance sensor integrated on a silicon photonic chip with a footprint of well below 1 mm^2. The integrated system comprises a heterodyne receiver structure with tunable power splitting ratio and on-chip photodetectors. The functionality of the device is demonstrated in a synthetic-wavelength interferometry experiment using frequency combs as optical sources. We obtain accurate and fast distance measurements with an unambiguity range of 3.75 mm, a root-mean-square error of 3.4 µm and acquisition times of 14 µs.

References and links

1. G. Ulbers, "A sensor for dimensional metrology with an interferometer using integrated optics technology," Measurement **9**(1), 13–16 (1991).
2. T. Oka, H. Nakajima, M. Tsugai, U. Hollenbach, U. Wallrabe, and J. Mohr, "Development of a micro-optical distance sensor," Sens. Actuators A Phys. **102**(3), 261–267 (2003).
3. M. Hochberg and T. Baehr-Jones, "Towards fabless silicon photonics," Nat. Photonics **4**(8), 492–494 (2010).
4. M. Hochberg, N. C. Harris, R. Ding, Y. Zhang, A. Novack, Z. Xuan, and T. Baehr-Jones, "Silicon Photonics: The Next Fabless Semiconductor Industry," IEEE Solid-State Circ. Mag. **5**(1), 48–58 (2013).
5. D. Hofstetter, H. P. Zappe, and R. Dandliker, "Optical displacement measurement with GaAs/AlGaAs-based monolithically integrated Michelson interferometers," J. Lightwave Technol. **15**(4), 663–670 (1997).
6. A. Rubiyanto, H. Herrmann, R. Ricken, F. Tian, and W. Sohler, "Integrated optical heterodyne interferometer in lithium niobate," J. Nonlinear Opt. Phys. Mater. **10**(2), 163–168 (2001).
7. H. Toda, M. Haruna, and H. Nishihara, "Integrated-optic heterodyne interferometer for displacement measurement," J. Lightwave Technol. **9**(5), 683–687 (1991).
8. Y. Li and R. Baets, "Homodyne laser Doppler vibrometer on silicon-on-insulator with integrated 90 degree optical hybrids," Opt. Express **21**(11), 13342–13350 (2013).
9. Y. Li, S. Verstuyft, G. Yurtsever, S. Keyvaninia, G. Roelkens, D. Van Thourhout, and R. Baets, "Heterodyne laser Doppler vibrometers integrated on silicon-on-insulator based on serrodyne thermo-optic frequency shifters," Appl. Opt. **52**(10), 2145–2152 (2013).
10. M. Lauermann, C. Weimann, A. Knopf, W. Heni, R. Palmer, S. Koeber, D. L. Elder, W. Bogaerts, J. Leuthold, L. R. Dalton, C. Rembe, W. Freude, and C. Koos, "Integrated optical frequency shifter in silicon-organic hybrid (SOH) technology," Opt. Express **24**(11), 11694–11707 (2016).
11. S. Schneider, M. Lauermann, P.-I. Dietrich, C. Weimann, W. Freude, and C. Koos, "Optical coherence tomography system mass-producible on a silicon photonic chip," Opt. Express **24**(2), 1573–1586 (2016).
12. D. B. Cole, C. Sorace-Agaskar, M. Moresco, G. Leake, D. Coolbaugh, and M. R. Watts, "Integrated heterodyne interferometer with on-chip modulators and detectors," Opt. Lett. **40**(13), 3097–3100 (2015).
13. F. Aflatouni, B. Abiri, A. Rekhi, and A. Hajimiri, "Nanophotonic coherent imager," Opt. Express **23**(4), 5117–5125 (2015).
14. T.-A. Liu, N. R. Newbury, and I. Coddington, "Sub-micron absolute distance measurements in sub-millisecond times with dual free-running femtosecond Er fiber-lasers," Opt. Express **19**(19), 18501–18509 (2011).
15. V. Ataie, P. P. Kuo, A. Wiberg, Z. Tong, C. Huynh, N. Alic, and S. Radic, "Ultrafast Absolute Ranging by Coherent Parametric Comb," in Optical Fiber Communication Conference 2013, OSA Technical Digest (online) (Optical Society of America, 2013), paper OTh3D.2.
16. C. Weimann, F. Hoeller, Y. Schleitzer, C. A. Diez, B. Spruck, W. Freude, Y. Boeck, and C. Koos, "Measurement of Length and Position with Frequency Combs," J. Phys. Conf. Ser. **605**, 012030 (2015).

17. D. Ganin, P. Trocha, M. Pfeiffer, M. Karpov, A. Kordts, J. Krockenberger, P. Marin-Palomo, S. Wolf, S. Randel, W. Freude, T. J. Kippenberg, and C. Koos, "Ultrafast Dual-Comb Distance Metrology Using Dissipative Kerr Solitons," in Conference on Lasers and Electro-Optics 2017, OSA Technical Digest (online) (Optical Society of America, 2017), paper STh4L.6.

18. C. Weimann, M. Lauermann, T. Fehrenbach, R. Palmer, F. Hoeller, W. Freude, and C. Koos, "Silicon Photonic Integrated Circuit for Fast Distance Measurement with Frequency Combs," in Conference on Lasers and Electro-Optics 2014, OSA Technical Digest (online) (Optical Society of America, 2014), paper STh4O.3.

19. T. Sakamoto, T. Kawanishi, and M. Izutsu, "Asymptotic formalism for ultraflat optical frequency comb generation using a Mach-Zehnder modulator," Opt. Lett. **32**(11), 1515–1517 (2007).

20. T. Sakamoto, T. Kawanishi, and M. Izutsu, "Widely wavelength-tunable ultra-flat frequency comb generation using conventional dual-drive Mach-Zehnder modulator," Electron. Lett. **43**(19), 1039–1040 (2007).

21. C. Weimann, P. C. Schindler, R. Palmer, S. Wolf, D. Bekele, D. Korn, J. Pfeifle, S. Koeber, R. Schmogrow, L. Alloatti, D. Elder, H. Yu, W. Bogaerts, L. R. Dalton, W. Freude, J. Leuthold, and C. Koos, "Silicon-organic hybrid (SOH) frequency comb sources for terabit/s data transmission," Opt. Express **22**(3), 3629–3637 (2014).

22. C. Koos, J. Leuthold, W. Freude, M. Kohl, L. Dalton, W. Bogaerts, A. L. Giesecke, M. Lauermann, A. Melikyan, S. Koeber, S. Wolf, C. Weimann, S. Muehlbrandt, K. Koehnle, J. Pfeifle, W. Hartmann, Y. Kutuvantavida, S. Ummethala, R. Palmer, D. Korn, L. Alloatti, P. C. Schindler, D. L. Elder, T. Wahlbrink, and J. Bolten, "Silicon-Organic Hybrid (SOH) and Plasmonic-Organic Hybrid (POH) Integration," J. Lightwave Technol. **34**(2), 256–268 (2016).

23. P. Marin-Palomo, J. N. Kemal, M. Karpov, A. Kordts, J. Pfeifle, M. H. P. Pfeiffer, P. Trocha, S. Wolf, V. Brasch, M. H. Anderson, R. Rosenberger, K. Vijayan, W. Freude, T. J. Kippenberg, and C. Koos, "Microresonator-based solitons for massively parallel coherent optical communications," Nature **546**(7657), 274–279 (2017).

24. V. Brasch, E. Lucas, J. D. Jost, M. Geiselmann, and T. J. Kippenberg, "Self-referenced photonic chip soliton Kerr frequency comb," Light Sci. Appl. **6**(1), e16202 (2016).

25. P. Trocha, D. Ganin, M. Karpov, M. H. P. Pfeiffer, A. Kordts, J. Krockenberger, S. Wolf, P. Marin-Palomo, C. Weimann, S. Randel, W. Freude, T. J. Kippenberg, and C. Koos, "Ultrafast optical ranging using microresonator soliton frequency combs," https://arXiv:1707.05969 (2017).

26. T. Baehr-Jones, R. Ding, A. Ayazi, T. Pinguet, M. Streshinsky, N. Harris, J. Li, L. He, M. Gould, and Y. Zhang, "A 25 Gb/s silicon photonics platform," https://arXiv:1203.0767 (2012).

27. C. Weimann, D. Meier, S. Wolf, Y. Schleitzer, M. Totzeck, A. Heinrich, F. Hoeller, J. Leuthold, W. Freude, and C. Koos, "Fast high-precision distance measurements on scattering technical surfaces using frequency combs," in Conference on Lasers and Electro-Optics 2013, OSA Technical Digest (online) (Optical Society of America, 2013), paper CTu2I.3.

28. I. Coddington, W. C. Swann, L. Nenadovic, and N. R. Newbury, "Rapid and precise absolute distance measurements at long range," Nat. Photonics **3**(6), 351–356 (2009).

29. G. Margheri, C. Giunti, S. Zatti, S. Manhart, and R. Maurer, "Double-wavelength superheterodyne interferometer for absolute ranging with submillimeter resolution: results obtained with a demonstration model by use of rough and reflective targets," Appl. Opt. **36**(25), 6211–6216 (1997).

30. X. Wang, S. Takahashi, K. Takamasu, and H. Matsumoto, "Spatial positioning measurements up to 150 m using temporal coherence of optical frequency comb," Precis. Eng. **37**(3), 635–639 (2013).

31. C. Weimann, M. Fratz, H. Wölfelschneider, W. Freude, H. Höfler, and C. Koos, "Synthetic-wavelength interferometry improved with frequency calibration and unambiguity range extension," Appl. Opt. **54**(20), 6334–6343 (2015).

32. C. Weimann, F. Hoeller, and C. Koos, "High-precision laser ranging for industrial metrology with dual-color electro-optic frequency combs," in 116th Annual DGaO Conference 2015, talk A4.

33. D. Vermeulen, Y. De Koninck, Y. Li, E. Lambert, W. Bogaerts, R. Baets, and G. Roelkens, "Reflectionless grating couplers for Silicon-on-Insulator photonic integrated circuits," Opt. Express **20**(20), 22278–22283 (2012).

34. Corning, SMF-28e + Optical Fiber Product Information, 2014.

35. R. E. Bartolo, A. B. Tveten, and A. Dandridge, "Thermal Phase Noise Measurements in Optical Fiber Interferometers," IEEE J. Quantum Electron. **48**(5), 720–727 (2012).

36. P.-E. Dupouy, M. Büchner, P. Paquier, G. Trénec, and J. Vigué, "Interferometric measurement of the temperature dependence of an index of refraction: application to fused silica," Appl. Opt. **49**(4), 678–682 (2010).

37. A. K. Melikov, U. Krüger, G. Zhou, T. L. Madsen, and G. Langkilde, "Air temperature fluctuations in rooms," Build. Environ. **32**(2), 101–114 (1997).

38. L. S. Schuetz, J. H. Cole, J. Jarzynski, N. Lagakos, and J. A. Bucaro, "Dynamic thermal response of single-mode optical fiber for interferometric sensors," Appl. Opt. **22**(3), 478–483 (1983).

39. U. Vry, "Absolute Statistical Error in Two-wavelength Rough-surface Interferometry (ROSI)," Opt. Acta: International Journal of Optics **33**(10), 1221–1225 (1986).

40. P. Pavliček and J. Soubusta, "Theoretical measurement uncertainty of white-light interferometry on rough surfaces," Appl. Opt. **42**(10), 1809–1813 (2003).

41. E. Baumann, J.-D. Deschênes, F. R. Giorgetta, W. C. Swann, I. Coddington, and N. R. Newbury, "Speckle phase noise in coherent laser ranging: fundamental precision limitations," Opt. Lett. **39**(16), 4776–4779 (2014).

42. M. R. Billah, T. Hoose, T. Onanuga, N. Lindenmann, P. Dietrich, T. Wingert, M. L. Goedecke, A. Hofmann, U. Troppenz, A. Sigmund, M. Möhrle, W. Freude, and C. Koos, "Multi-Chip Integration of Lasers and Silicon Photonics by Photonic Wire Bonding," in Conference on Lasers and Electro-Optics 2015, OSA Technical Digest (online) (Optical Society of America, 2015), paper STu2F.2.
43. N. Lindenmann, S. Dottermusch, M. L. Goedecke, T. Hoose, M. R. Billah, T. P. Onanuga, A. Hofmann, W. Freude, and C. Koos, "Connecting Silicon Photonic Circuits to Multicore Fibers by Photonic Wire Bonding," J. Lightwave Technol. **33**(4), 755–760 (2015).
44. N. Lindenmann, G. Balthasar, D. Hillerkuss, R. Schmogrow, M. Jordan, J. Leuthold, W. Freude, and C. Koos, "Photonic wire bonding: a novel concept for chip-scale interconnects," Opt. Express **20**(16), 17667–17677 (2012).
45. J. Ronnau, S. Haimov, and S. P. Gogineni, "The effect of signal-to-noise ratio on phase measurements with polarimetric radars," Remote Sens. Rev. **9**(1-2), 27–37 (1994).
46. P. R. Bevington and D. K. Robinson, *Data reduction and error analysis for the physical sciences*, 3rd ed. (McGraw-Hill, 2003).

1. Introduction

High-precision distance sensors are of great importance for a wide range of applications such as inline inspection of mechanical parts or precise referencing of translation axes in industrial machinery. These sensors need to be compact, robust, and capable of providing absolute distance measurements with single-digit micrometer accuracy and short acquisition times. So far, miniaturization of optical sensors has mainly been achieved by emulating conventional macroscopic optical configurations using discrete micro-optical components such as microlenses and micro-optical benches [1,2]. These schemes, however, require costly assembly and highly precise alignment of a multitude of components and are therefore not well suited for mass production. At the same time, photonic integrated circuits (PIC) have gained considerable maturity. Silicon photonics emerges as a particularly attractive platform, lending itself to large-scale photonic-electronic integration on the basis of mature high-yield CMOS processes that are offered by widely available foundry services [3,4]. Photonic integration is currently mainly driven by data- and telecommunication applications such as high-speed optical interconnects, but it is indisputable that there is also large application potential for PIC in optical sensing and metrology. However, while early demonstrations of PIC for interferometric distance measurements made use of GaAs/AlGaAs and Lithium-Niobate ($LiNbO_3$) as integration platform [5–7], there are only very few examples where large-scale silicon photonic integration has been exploited for applications in optical metrology. Using the silicon-on-insulator (SOI) platform, Laser Doppler vibrometers and optical frequency shifters have been demonstrated [8–10] and an optical coherence tomography system has been realized [11]. An integrated heterodyne interferometer for measurements of relative displacements with a standard deviation of 2 nm was demonstrated in [12]. However, like all optical single-wavelength interferometric schemes, this approach is limited to an unambiguity range of half the optical wavelength, i.e., approximately 775 nm, which prohibits its use for many applications in industrial metrology. A silicon PIC for absolute distance measurements with an electrically-generated laser frequency chirp was demonstrated in [13], achieving a depth resolution of 15 μm for an acquisition time of 500 μs. While this represents an important demonstration, the approach cannot yet fulfill the requirement of sub-10 μm measurement accuracy in conjunction with measurement rates well in excess of 10 kHz that are associated with many applications in industrial high-precision metrology. Measurement principles based on optical frequency combs have recently shown to deliver the sought-after combination of precision and measurement speed [14–17]. However, these works employ classical macroscopic optical setups, e.g. using fiber-optical components.

In this paper, we expand on our previous work [18] and demonstrate a silicon-on-insulator PIC for fast and precise absolute distance measurements using a pair of frequency combs (FC) as optical sources for multi-heterodyne synthetic-wavelength interferometry. The precisely known frequency spacing of the comb lines provides a number of precisely known synthetic wavelengths, the phases of which can be measured simultaneously via heterodyne detection with a detuned optical frequency comb used as a local oscillator. The combination

of a dual-comb measurement scheme with photonic integration on silicon presented in this paper results in a fast, precise and very compact optical distance sensor. We achieve standard deviations of less than 5 μm for an acquisition time of 14 μs, enabling measurement rates well beyond 50 kHz. Our system consists of a heterodyne interferometer, comprising a multitude of components such as power splitters and waveguides as well as phase shifters and photodetectors, all integrated into a single silicon PIC covering an on-chip footprint of 0.25 mm². An on-chip tunable power splitter (TPS) is used to distribute the available power of the local oscillator in an optimum way. The PIC relies entirely on the standard device portfolio offered by a silicon photonic foundry and does not require any customized components or fabrication steps. The FC are generated externally by modulating cw lasers with standard telecom-grade dual-drive Mach-Zehnder modulators (MZM). The MZM are driven by fixed-frequency sinusoidal electrical signals in push-push operation to generate frequency combs that typically comprise 5 – 20 equidistant lines [19,20]. In future implementations, silicon receiver PIC may be monolithically co-integrated with high-performance frequency comb generators using the silicon-organic hybrid (SOH) approach [21,22]. Moreover, when combined with ultrabroadband Kerr comb generators in a hybrid multi-chip assembly, such silicon receiver PIC will pave the path towards ultra-fast high-precision distance measurements with chip-scale systems [17,23–25].

2. Experimental setup with silicon photonic chip and measurement principle

A schematic of the experimental setup is depicted in Fig. 1(a). Light from a continuous wave (cw) laser with a wavelength $\lambda_0 = 1550\,\text{nm}$ is amplified to a power of 18 dBm in an erbium-doped fiber amplifier (EDFA), then split by a fiber coupler, and fed into a pair of Mach-Zehnder modulators (MZM) for frequency comb generation (FC 1 and FC 2). The use of a central wavelength within the C band (1530 nm – 1565 nm), which is commonly used for fiber-optic telecommunication, allows to employ commercially widely available components as well as to make use of the standard device portfolio offered by any silicon foundry. The lithium-niobate MZM are driven by sinusoidal electrical signals at frequencies of $f_{\text{mod,LO}} = 40.000\,\text{GHz}$ for FC 1 and $f_{\text{mod,sig}} = 39.957\,\text{GHz}$ for FC 2. The corresponding modulation depth amounts to 1.5π. The phase-modulated light exhibits a comb-like spectrum with a line spacing precisely defined by the respective driving frequency, Insets (I) and (II) in Fig. 1(a). By adjusting the bias voltage, the relative phase and the amplitudes of the driving signals between both arms of the modulator, the frequency combs are spectrally flattened [19,20]. Both MZM are temperature-stabilized via thermoelectric coolers and their corresponding controllers, ensuring stable bias points. We did not measure the time-dependency of the comb spectra, but we could not observe any short-term or long-term degradation of the flatness of the spectral envelope of the frequency combs during our experiments. FC 1 is additionally frequency-shifted by $\Delta f_0 = 55\,\text{MHz}$ using an acousto-optic modulator (AOM). The FC are coupled to the PIC using a fiber array and grating couplers. FC 2 enters the PIC at the port marked by (1) in Fig. 1. A multimode interference coupler (MMI) is used to split the comb into two parts. One part of FC 2 is directly guided to the reference detector, the other part exits the chip again at port (2), is guided to the measurement path and emitted by a collimator towards the measurement target, here represented by a mirror. After back-and-forth propagation over the measurement distance z, this part of FC 2 is coupled back to the PIC through port (4) and fed to the measurement detector. FC 1 enters the PIC at port (3) and is distributed to both measurement and reference detector via a power splitter with tunable splitting ratio (tunable power splitter, TPS). The TPS is realized by *p-i-n* phase shifters in a MZM configuration and allows for a flexible power distribution of FC 1 on both detectors. The detectors consist of vertical Germanium *p-i-n* junctions [26] and are realized as balanced photodetectors for optimum suppression of common-mode signal components.
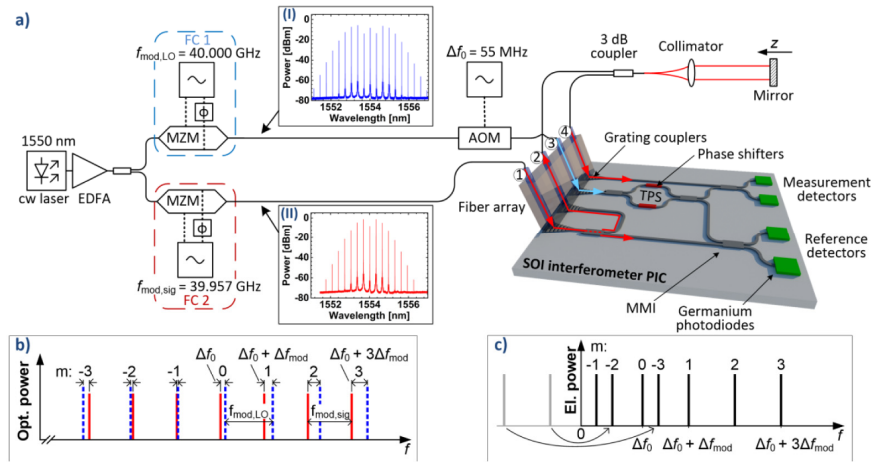
Fig. 1. Experimental setup and detection principle. (a) Light from a cw laser is amplified in an erbium-doped fiber amplifier (EDFA) to a power of 18 dBm, split, and directed to two MZM. Two slightly detuned frequency combs (FC 1 and FC 2, see insets I and II for optical spectra) with a line spacing of $f_{mod,LO} = 40.000\,GHz$ and $f_{mod,sig} = 39.957\,GHz$ are generated by sinusoidal phase modulation. FC 1 is additionally shifted by $\Delta f_0 = 55\,MHz$ in an acousto-optical modulator (AOM). Light is coupled to and from the silicon PIC via a fiber array and grating couplers. FC 1 is coupled to the PIC through port 3, and is further distributed by a tunable power splitter (TPS) to the measurement and the reference detector, where it acts as local oscillator (LO) for multi-heterodyne detection of FC 2. FC 2 is coupled to the PIC though port 1 and split by a multimode interference coupler (MMI). One part of FC 2 is guided directly to the reference detector, where it is superimposed with FC 1. The other part exits the PIC through port 3, is guided via single-mode fibers to a collimator and propagates over the free-space measurement path of length z. The reflected light is coupled back into the fiber, sent to the PIC through port 4, and finally superimposed with FC 1 on the measurement detectors. (b) Schematic optical power spectra of FC 1 (dashed blue lines) and FC 2 (continuous red lines). The line spacings of FC 1 and FC 2 are slightly detuned by $\Delta f_{mod} = |f_{mod,LO} - f_{mod,sig}|$, and the center frequencies are offset by Δf_0. (c) Schematic one-sided power spectrum of the photocurrent (negative frequencies grayed out). Quadratic detection of FC 1 and FC 2 by a photodiode leads to a multitude of sinusoidal IF signals with frequencies $|\Delta f_0 + m\Delta f_{mod}|$ in the photocurrent (heterodyne detection). Negative frequencies of the corresponding two-sided spectrum are drawn in gray and mirrored to positive frequencies of the one-sided spectrum. The phases of the IF signals are directly linked to the phase shifts accumulated by the lines of the FC during propagation.

A microscopic image of the PIC is depicted in Fig. 2. The occupied on-chip area of all elements amounts to $0.25\,mm^2$.

FC 1 serves as local oscillator (LO) for heterodyne detection of FC 2, which is further also called signal comb. The line spacing of FC 1 is detuned by $\Delta f_{mod} = 43\,MHz$ and its center frequency is detuned by $\Delta f_0 = 55\,MHz$ with respect to FC 2, as illustrated in Fig. 1(b). The comb lines of FC 1 and FC 2 are superimposed on the balanced photodetectors and quadratic detection leads to a multitude of sinusoidal photocurrents at distinct intermediate frequencies (IF) in the baseband. With an integer m denoting the order of the comb lines, the photocurrent shows N spectral lines at frequencies $|\Delta f_0 + m\Delta f_{mod}|$, as depicted schematically in Fig. 1(c). A rigorous mathematical description of the measurement scheme can be found in Appendix A.

To find the distance z to the mirror, the spectrum of the photocurrent is analyzed. The phases of the IF beat notes are directly linked to the phase shifts that the FC accumulate during their propagation to the respective detectors. The measurement distance z is extracted from the IF phase differences between reference and measurement detectors [16,27,28].
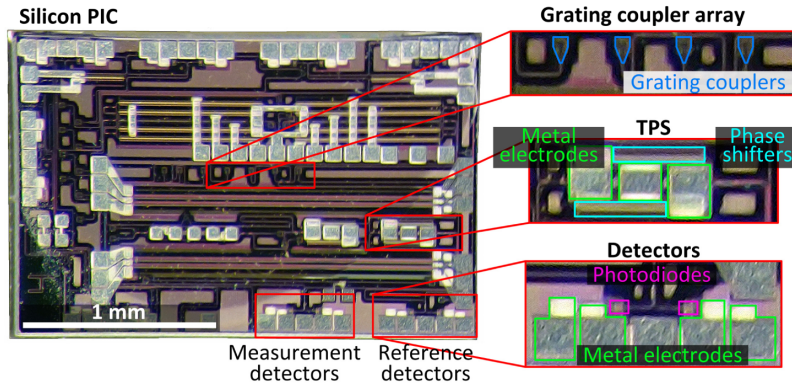
Fig. 2. Microscope image of the silicon PIC. The main elements used by the distance sensor system are highlighted by colored frames and depicted magnified on the right-hand side. Connecting waveguides are routed between additional optical circuits for other purposes, which are co-integrated on the same chip. The occupied on-chip area of the distance sensor system amounts to 0.25 mm^2.

With the exception of the measurement distance z, all other optical path lengths in the system are fixed. Their influence on the phases can be removed by a calibration measurement (for details see Appendix A). The phase differences $\Delta\varphi_m$ between reference and measurement detector are linked to the distance z by the propagators $\exp\left(-\mathrm{j}\omega_{m,\mathrm{sig}}2z/c\right)$ of the reflected signal comb lines m of FC 2 with (angular) frequency $\omega_{m,\mathrm{sig}} = 2\pi f_{m,\mathrm{sig}} = 2\pi\left(f_{0,\mathrm{sig}} + mf_{\mathrm{mod,sig}}\right)$, where $f_{0,\mathrm{sig}} = c/\lambda_0$ is defined by the input cw laser and c is the vacuum speed of light. As described in Eq. (14) of Appendix A, the unwrapped phase differences of the IF signals with respect to a calibration at z_0 can be expressed as

$$\delta\varphi_m(z) = \Delta\varphi_m(z) - \Delta\varphi_m(z_0) = 2(z-z_0)m\,\omega_{\mathrm{mod,sig}}\big/c + 2(z-z_0)\,\omega_{0,\mathrm{sig}}\big/c. \qquad (1)$$

The last term in Eq. (1) corresponds to the phase evaluated in classical interferometry at an optical wavelength $\lambda_0 = 2\pi c\omega_{0,\mathrm{sig}}^{-1}$. However, due to the 2π-periodicity of the phase and the back-and-forth propagation to the mirror, this would only provide an unambiguity range of $\lambda_0/2 = 775\,\mathrm{nm}$. Additionally, drifts of the laser wavelength would introduce errors. The first term in Eq. (1), however, corresponds to the phases evaluated in interferometry with so-called synthetic wavelengths $\Lambda_m = 2\pi c\left(m\omega_{\mathrm{mod,sig}}\right)^{-1}$ [29], see Appendix A. This considerably extends the unambiguity range to $\Lambda_1/2 = 3.75\,\mathrm{mm}$, while at the same time the measurement result is traceable to the stability of the electronically provided drive frequency $\omega_{\mathrm{mod,sig}}$. The unambiguity range could be extended further by, e.g., subsequent measurements with different comb line spacings [28,30], or by a combination with longer-range time-of-flight measurement schemes [31]. To extract the information contained in the N-1 synthetic wavelengths provided simultaneously by the use of a frequency comb, the slope with respect to m is calculated from Eq. (1),

$$\frac{\mathrm{d}\delta\varphi_m(z)}{\mathrm{d}m} = 2\left(z-z_0\right)\frac{\omega_{\mathrm{mod,sig}}}{c}. \qquad (2)$$

As $\omega_{\mathrm{mod,sig}}$ and c are accurately known, the distance z with respect to a calibration position z_0 can be precisely determined. This approach is illustrated in Fig. 3. The measured IF power
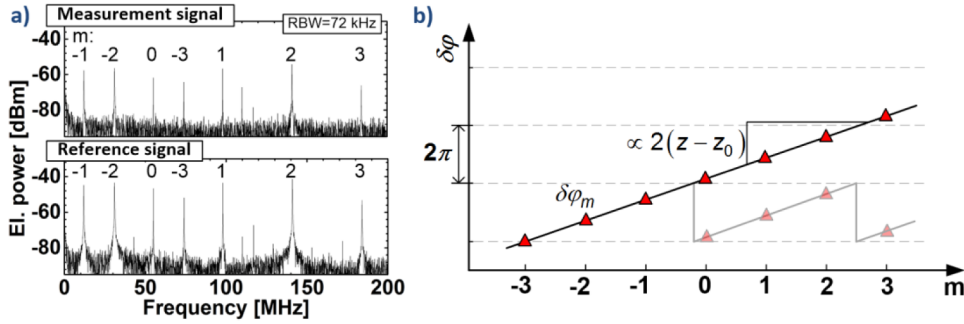
Fig. 3. Data processing for dual-comb synthetic-wavelength interferometry. (a) Measured one-sided spectrum of the photocurrents of measurement and reference detectors acquired at a resolution bandwidth (RBW) of 72 kHz. The IF lines are indexed by m as in Fig. 1. Lines with index $m < -1$, that, in the present configuration, would appear at negative frequencies in the two-sided electrical power spectrum, are mirrored to the positive frequency range in the one-sided spectrum as explained in Fig. 1 (c). (b) Differences of the IF phases $\delta\varphi_m$ as measured between the reference and the measurement detectors as a function of the line index m. Phase values before unwrapping (sawtooth-like shapes) are depicted in light colors, illustrating the 2π-periodicity. The unwrapped phase values follow a linear relationship. The slope of the fitted straight line is proportional to the optical path length difference between reference and measurement paths, see Eq. (2).

spectra for both measurement and reference detector are depicted in Fig. 3(a), showing the evaluated 7 lines with $m = -3, \ldots, 0, \ldots, 3$. The heterodyne detection scheme with a slightly detuned LO comb (FC 1) allows sampling of an optical bandwidth of $(7-1) \times 40\,\text{GHz} = 240\,\text{GHz}$ with an electrical bandwidth of less than 200 MHz.

The phases of the individual beat notes are extracted by performing a discrete Fourier transform (DFT) after analog-to-digital conversion (A/D) of the IF signals with a resolution of 12 bit and sample rate of 3.6 GS/s. The DFT operates on 5×10^4 samples per channel, which corresponds to an acquisition time of 14 μs. The slope of the unwrapped phase differences is determined by a linear regression, as illustrated in Fig. 3(b), and is proportional to the measurement distance $z - z_0$. The signal processing steps to extract the measurement distance can be realized efficiently on an FPGA to enable real-time operation [32].

3. Measurement results

For performance characterization, we measure the distance to a plane mirror mounted on a motorized translation stage. The stage has a feedback-controlled positioning accuracy of 50 nm and serves as a reference for our distance measurements. The power emitted into free space amounts to −4.5 dBm. The distance measurement results are shown in Fig. 4(a). The unwrapped measured distance z is plotted as function of the distance set on the translation stage z_{set}, see blue crosses in Fig. 4(a). Each distance measurement corresponds to an acquisition time of 14 μs. The mean of the distance error z-z_{set} is calculated from 10 subsequent measurements at the same position, see black dots in Fig. 4(a). Error bars indicate a range of twice the standard deviation. The absolute value of the mean error stays below 4 μm, while the standard deviation stays below 5 μm for all positions. The root-mean-square position error calculated over the whole measurement range amounts to 3.4 μm. The small deviations of the mean distance error from 0 μm are partly due to thermal path length fluctuations in the optical fibers used in the current measurement setup and partly due to crosstalk caused by reflections from on-chip devices such as MMI or grating couplers. While the latter can be alleviated by using devices with low back-reflection [33], we further analyze the effect of thermal path length fluctuations. The systematic error due to thermally varying optical path length differences ΔD inside the optical fibers with a geometric length of L is
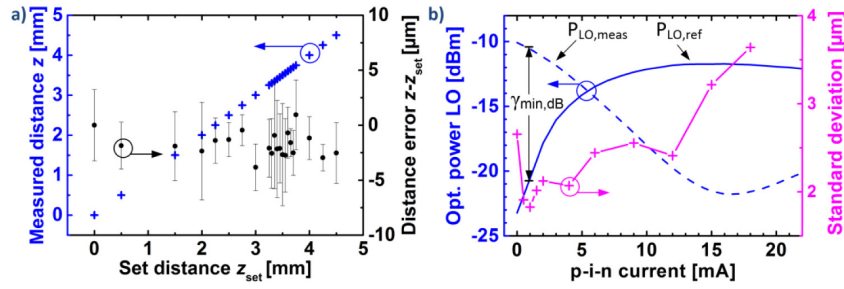
Fig. 4. Measurement results. (a) Unwrapped measured distances z (blue) and errors z-z_{set} (black) vs. set distance z_{set}. Error bars indicated a range of twice the standard deviation obtained from 10 subsequent measurements at the same position. Acquisition time per measurement is 14 μs. The accuracy of the positioning stage used for setting the distance z_{set} is specified to be better than 50 nm. The small deviations of the mean distance error from 0 μm are attributed to thermal path length fluctuations in the optical fibers and to crosstalk caused by reflections from on-chip devices such as MMI or grating couplers. (b) Optical power of FC 1 (LO) at measurement and reference detector ($P_{LO,meas}$ and $P_{LO,ref}$ along with corresponding standard deviation for the distance measurement, both plotted vs. the current of the p-i-n phase shifter in the TPS. The power splitting ratio resulting in minimum standard deviation is indicated by $\gamma_{min,dB}$.

estimated in the following using published data. The group refractive index is denoted as n, the thermo-optic coefficient as $\mathrm{d}n/\mathrm{d}T$, the thermal expansion coefficient as $\alpha_L = (\mathrm{d}L/\mathrm{d}T)/L$ and the length-averaged temporal temperature difference of the optical fibers as ΔT. The optical path length $D = nL$ varies with temperature according to $\mathrm{d}D = (n\,\mathrm{d}(L)/\mathrm{d}T + L\,\mathrm{d}(n)/\mathrm{d}T)\mathrm{d}T$. With the previous definitions, the temperature-induced optical path length variations are given as

$$\Delta D = \left(n\alpha_L + \frac{\mathrm{d}n}{\mathrm{d}T} \right) L \Delta T \tag{3}$$

With $n = 1.4679$ [34], $\alpha_L \approx 0.5 \times 10^{-6}\,\mathrm{K}^{-1}$ [35] and $\mathrm{d}n/\mathrm{d}T \approx 10 \times 10^{-6}\,\mathrm{K}^{-1}$ [35,36], the relative optical path length change amounts to

$$(\Delta D/\Delta T)/L = 10.7\,\mathrm{\mu m}/(\mathrm{K\,m}) \tag{4}$$

Typical room temperature fluctuations during the time period of approximately 1 min needed to move the measurement target to the next position are approximately $\Delta T = 0.1\,\mathrm{K}$ [37]. The dynamic thermal response of a standard Hytrel jacketed single-mode optical fiber has a 3 dB bandwidth of roughly 10 Hz [38] and thus the temperature of the fiber is expected to follow the temperature fluctuations of the room temperature on this time scale. With Eq. (4) and the geometric fiber length of $L = 5\,\mathrm{m}$ used in our experiment, we expect systematic deviations in the order of $\Delta D \approx 5\,\mathrm{\mu m}$, which fits well to the experimentally observed deviations of the mean values, see Fig. 4(a). This systematic error source can be overcome by reduced fiber lengths, by active compensation, e.g., by a simultaneous calibration measurement at a second center wavelength [32], or by full integration of the sensor system on the chip, which, due to its low mass and volume, could potentially be temperature-stabilized without great technical effort.

A mirror was used as a measurement target for the presented characterization measurements, but in principle also optically rough surfaces could be measured, albeit at a reduced precision due to decreased signal-to-noise power ratio and because of speckle-induced phase noise [39–41]. The influence of the tunable power splitter (TPS) can be seen in
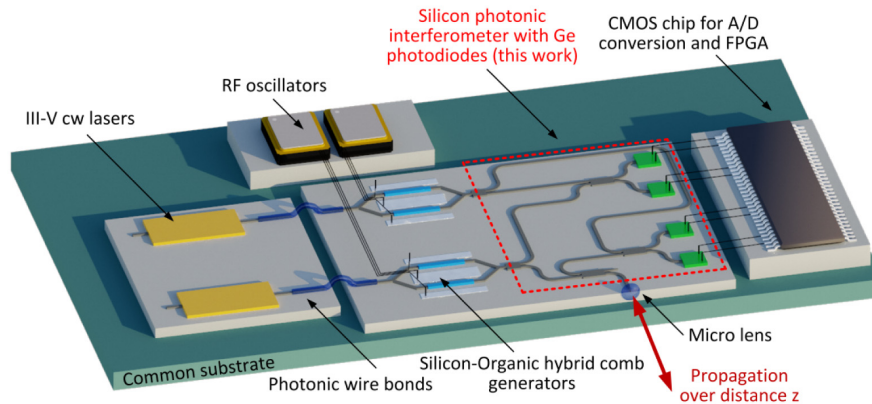
Fig. 5. Vision of a future chip-scale distance measurement system. The photonic elements comprise light sources (III-V cw lasers), frequency comb generators realized by silicon-organic hybrid (SOH) modulators [21,22], and an interferometer with photo detectors, as demonstrated in this work. The electronic components comprise a DC voltage supply (not depicted), RF oscillators for driving the comb generators, and readout and processing circuitry, e.g., A/D converters connected to an FPGA. The individual elements are assembled on a common submount. Electrical connections are realized by standard wire bonding techniques. Light is routed by single-mode on-chip waveguides and by photonic wire bonds, the latter being fabricated by direct-write three-dimensional two-photon lithography [42–44]. Using the same fabrication technique, tailored free-form micro lens can be printed directly to the facet of the optical chip to collimate the light radiated to and from the chip edge [11].

Figure 4(b). The measured optical powers of the LO comb FC 1 arriving at the reference detector and the measurement detector are plotted in blue as a function of the current applied to the *p-i-n* phase shifter in one arm of the TPS. The standard deviation for repeated measurements is plotted in magenta. The power splitting ratio γ_{dB} can be adjusted via the current through the *p-i-n* phase shifter to yield the lowest standard deviation for given power levels. The optical power of signal comb FC 2 arriving at the measurement detector $P_{sig,meas}$ is subject to additional power losses $\eta = P_{sig,meas}/P_{sig,ref}$ compared to the power $P_{sig,ref}$ of the signal comb arriving at the reference detector. With total grating coupler losses of 2×5 dB, free-space-to-fiber coupling losses of 7 dB, and the 6 dB loss for propagating twice through an additional 3 dB coupler, the additional loss amounts to $\eta_{dB} = 10\lg(\eta) = -23\,\text{dB}$. To compensate this lower signal power arriving at the measurement detector, the TPS is set in a way that most of the power of the LO comb FC 1 is distributed to the measurement detector. The input power into the TPS is denoted P_{LO}, the power splitting ratio is denoted γ. The two optical power levels $P_{LO,ref} = \gamma P_{LO}$, and $P_{LO,meas} = (1-\gamma)P_{LO}$ denote the optical powers of the LO comb FC 1 arriving at the reference detector and the measurement detector, respectively. Experimentally, we find a value of $\gamma_{min,dB} = 10\lg(\gamma_{min}) = -10.2\,\text{dB}$ to result in the minimum standard deviation and use this value for the characterization measurements. This is close to the theoretical optimum value of $\gamma_{min,dB,theo} = -11.8\,\text{dB}$ obtained for a measurement path loss of $\eta_{dB} = -23\,\text{dB}$, see Appendix B. For other measurement path losses, the splitting ratio can be dynamically adapted to always operate at optimum conditions. It is a strong advantage of photonic integration that such functionalities can be realized at virtually no additional cost.

4. Vision for further photonic integration

Our vision of a future fully integrated distance sensor system is illustrated in Fig. 5. The envisaged sensor consists of a multi-chip assembly where electronic and photonic wire bonds [42–44] are used to connect the individual chips. This approach allows to combine the distinct

advantages of complementary photonic integration platforms: The cw carriers can be provided by III-V semiconductor lasers and FC can be generated by sinusoidal phase modulation in highly efficient silicon-organic hybrid (SOH) comb generators [21,22], driven by conventional RF oscillators with slightly detuned frequencies. Signal splitting and combining as well as heterodyne detection can be accomplished by the standard silicon photonic device portfolio, comprising also on-chip Germanium photodiodes. For coupling of light to and from the measurement path, chip-attached micro lenses could be used, fabricated by the same direct-write three-dimensional two-photon lithography used for photonic wire bonding [11]. Read-out and processing of electric signals is realized with standard electronic components connected through electrical wirebonds. As a specific advantage of the hybrid integration approach, the scheme can easily be adapted for use with other chip-scale comb sources such as ultrabroadband Kerr comb generators which could further enhance the performance [17]. We see the main challenges in the minimizing the optical insertion losses, in realizing of a cost-effective packaging for hybrid integration, and in fabricating miniaturized comb sources. In general, chip-scale sensor systems stand out due to their ultra-compact footprint, which is an important asset for many applications. Moreover, the devices are mechanically robust and lend themselves to massive parallelization, e.g., by integrating a multitude of measurement channels on a single photonic chip.

5. Summary

We demonstrated an integrated silicon PIC capable of fast and accurate distance measurement with 3.75 mm unambiguity range using the concept of synthetic-wavelength interferometry with externally generated frequency combs. A root-mean-square error of 3.4 µm is achieved for an acquisition time of 14 µs. The PIC covers an on-chip footprint of approximately 0.25 mm^2 and relies entirely on the standard device portfolio offered by a silicon photonic foundry. There are many possibilities to further extend the concept, such as co-integration of lasers sources, comb generators [21] or electronics. We believe that large-scale photonic integration will enable completely new sensing and measurement systems of unprecedented scalability and functionality in the near future.

Appendix A: Mathematical description of measurement scheme

In the following section, we give a rigorous mathematical description of the measurement scheme, which relies on quadratic detection of two detuned frequency combs by the measurement and reference detector. Analytical signals $\underline{E}(t)$ are used to describe the time-domain electric fields, with the real part of the analytical signal representing the physically relevant field, $E(t) = \Re\{\underline{E}(t)\}$. The optical power is then given by $P = Z_0^{-1}\left\langle E^2(t) \right\rangle$, where $\langle - \rangle$ denotes the average over a few cycles of the optical carrier and where $Z_0 = 376.7\ \Omega$ represents the wave impedance of free space. In a first step we consider the measurement detector only. In accordance to the system detailed in Fig. 1(a), we consider the complex optical amplitudes $\underline{E}_{\text{sig,meas}}$ for the signal comb FC 2 arriving at the measurement detector. Each signal comb line l has an (angular) optical frequency $\omega_{l,\text{sig}}$,

$$\omega_{l,\text{sig}} = \omega_{0,\text{sig}} + l\omega_{\text{mod,sig}}. \tag{5}$$

The amplitudes of the signal comb lines are denoted as $\hat{\underline{E}}_{l,\text{sig,meas}}$, and the associated optical path length to the detector amounts to $2z + D_{\text{sig,meas}}$, where $D_{\text{sig,meas}}$ denotes the optical path length through the measurement setup to and from the origin $z = 0$ of the measurement coordinate system. Similarly, the complex optical amplitudes of the LO comb FC 1 at the

measurement detector are denoted as $\underline{E}_{\text{LO,meas}}$, and each comb line m has an (angular) optical frequency $\omega_{m,\text{LO}}$,

$$\omega_{m,\text{LO}} = \omega_{0,\text{LO}} + m\omega_{\text{mod,LO}} = \left(\omega_{0,\text{sig}} + \Delta\omega_0\right) + m\left(\omega_{\text{mod,sig}} + \Delta\omega_{\text{mod}}\right) \tag{6}$$

with a center frequency detuning $\Delta\omega_0$, a detuning of the line spacing of $\Delta\omega_{\text{mod}}$, and an amplitude $\hat{E}_{m,\text{LO,meas}}$. The LO comb arrives at the measurement detector after propagation over the optical path length $D_{\text{LO,meas}}$, which is entirely located within the measurement setup. The complex amplitudes of the two FC at the measurement detector are then given as

$$\underline{E}_{\text{sig,meas}}(t) = \sum_l \hat{E}_{l,\text{sig,meas}} \exp\left(j\omega_{l,\text{sig}}t\right)\exp\left(-j\left(2z + D_{\text{sig,meas}}\right)\omega_{l,\text{sig}}/c\right)$$

$$\underline{E}_{\text{LO,meas}}(t) = \sum_m \hat{E}_{m,\text{LO,meas}} \exp\left(j\omega_{m,\text{LO}}t\right)\exp\left(-jD_{\text{LO,meas}}\omega_{m,\text{LO}}/c\right). \tag{7}$$

The superposition of the signal and LO comb on the measurement detector with sensitivity S leads to a photocurrent containing multiple IF tones. The AC-part of the photocurrent $i_{\text{AC,meas}}$ of the measurement detector is given by

$$i_{\text{AC,meas}}(t) = Z_0^{-1}S \cdot \Re\left\{\underline{E}_{\text{sig,meas}}(t)^* \underline{E}_{\text{LO,meas}}(t)\right\}$$

$$= Z_0^{-1}S \cdot \Re\left\{\begin{array}{l}\displaystyle\sum_l\sum_m \hat{E}_{l,\text{sig,meas}}\hat{E}_{m,\text{LO,meas}} \\[2mm] \cdot \exp\left(j\left(\Delta\omega_0 + (m-l)\omega_{\text{mod,sig}} + m\Delta\omega_{\text{mod}}\right)t\right) \\[2mm] \cdot \exp\left(j\left(\left(2z + D_{\text{sig,meas}}\right)\omega_{l,\text{sig}} - D_{\text{LO,meas}}\omega_{m,\text{LO}}\right)/c\right)\end{array}\right\}. \tag{8}$$

The AC-part of the photocurrent $i_{\text{AC,ref}}$ of the reference detector can be derived in an analogous way by replacing "meas" by "ref" in the subscript,

$$i_{\text{AC,ref}}(t) = Z_0^{-1}S \cdot \Re\left\{\underline{E}_{\text{sig,ref}}(t)^* \underline{E}_{\text{LO,ref}}(t)\right\}$$

$$= Z_0^{-1}S \cdot \Re\left\{\begin{array}{l}\displaystyle\sum_l\sum_m \hat{E}_{l,\text{sig,ref}}\hat{E}_{m,\text{LO,ref}} \\[2mm] \cdot \exp\left(j\left(\Delta\omega_0 + (m-l)\omega_{\text{mod,sig}} + m\Delta\omega_{\text{mod}}\right)t\right) \\[2mm] \cdot \exp\left(j\left(D_{\text{sig,ref}}\omega_{l,\text{sig}} - D_{\text{LO,ref}}\omega_{m,\text{LO}}\right)/c\right)\end{array}\right\}. \tag{9}$$

In this relation, the quantities $D_{\text{sig,ref}}$ and $D_{\text{LO,ref}}$ denote the optical path lengths between the respective combs source and the reference detector. Note that, in contrast to Eq. (8) the external measurement distance $2z$ does not appear in the reference path length.

The frequency detunings $\Delta f_0 = \Delta\omega_0/(2\pi)$ and $\Delta f_{\text{mod}} = \Delta\omega_{\text{mod}}/(2\pi)$ amount to tens of megahertz and are small compared to the line spacing $f_{\text{mod,sig}} = \omega_{\text{mod,sig}}/(2\pi)$ of roughly 40 GHz. In theory, the photocurrent spectrum shows beat signals at distinct intermediate frequencies $f_{m,l}$,

$$f_{m,l} = \left|\Delta f_0 + (m-l)f_{\text{mod,sig}} + m\Delta f_{\text{mod}}\right|. \tag{10}$$

However, only a subset of these lines can actually be acquired by the photodetector and the subsequent A/D converter. For the FC deployed in our experiments, the analog bandwidth B

of the A/D converter used to record the signals amounts to 1.3 GHz and is much smaller than the ~40 GHz line spacing of the frequency combs, $B \Box f_{\mathrm{mod,sig}} \approx f_{\mathrm{mod,LO}}$. Moreover, the number of comb lines is limited such that $m\Delta f_{\mathrm{mod,LO}} \Box f_{\mathrm{mod,sig}} \approx f_{\mathrm{mod,LO}}$ for all comb line indices m.

As a consequence, for a given LO comb line m, only the beat note with the corresponding signal comb of same index $m = l$ is visible in the photocurrent. IF lines are hence found at distinct frequencies $f_{\mathrm{IF},m} = \left| \Delta f_0 + m \Delta f_{\mathrm{mod}} \right|$. The corresponding phases $\varphi_{m,\mathrm{meas}}$ of the IF lines at the measurement detector can be derived from Eq. (8),

$$
\begin{aligned}
\varphi_{m,\mathrm{meas}}\left(2z + D_{\mathrm{sig,meas}}, D_{\mathrm{LO,meas}}\right) &= \left(\left(2z + D_{\mathrm{sig,meas}}\right)\omega_{m,\mathrm{sig}} - D_{\mathrm{LO,meas}}\omega_{m,\mathrm{LO}}\right)\Big/c \\
&= \left(\left(2z + D_{\mathrm{sig,meas}}\right) - D_{\mathrm{LO,meas}}\right)\left(\omega_{0,\mathrm{sig}} + m\omega_{\mathrm{mod,sig}}\right)\Big/c \\
&\quad - D_{\mathrm{LO,meas}}\left(\Delta\omega_0 + m\Delta\omega_{\mathrm{mod}}\right)\Big/c \\
&= 2\pi\left(\left(2z + D_{\mathrm{sig,meas}}\right) - D_{\mathrm{LO,meas}}\right)\Lambda_m^{-1} \\
&\quad + 2\pi\left(\left(2z + D_{\mathrm{sig,meas}}\right) - D_{\mathrm{LO,meas}}\right)\lambda_{0,\mathrm{sig}}^{-1} \\
&\quad - D_{\mathrm{LO,meas}}\left(\Delta\omega_0 + m\Delta\omega_{\mathrm{mod}}\right)\Big/c.
\end{aligned}
\tag{11}
$$

The last part of Eq. (11) contains the so-called synthetic wavelength $\Lambda_m = c\left(mf_{\mathrm{mod,sig}}\right)^{-1}$ and shows the relation to classical interferometry with a single optical wavelength λ, where the phase shift φ experienced by an optical signal after propagation over the optical path length D is determined by $\varphi = 2\pi D\lambda^{-1}$. The beat signals at the reference detector have the exactly same frequencies as the beat signals at the measurement detector and serve as phase references. Their phases are determined analogously to Eq. (11) and are given as

$$
\varphi_{m,\mathrm{ref}}\left(D_{\mathrm{sig,ref}}, D_{\mathrm{LO,ref}}\right) = \left(D_{\mathrm{sig,ref}}\omega_{m,\mathrm{sig}} - D_{\mathrm{LO,ref}}\omega_{m,\mathrm{LO}}\right)\Big/c
\tag{12}
$$

The phase difference of the beat signals is given by:

$$
\begin{aligned}
\Delta\varphi_m(z) &= \varphi_{m,\mathrm{meas}}\left(2z + D_{\mathrm{sig,meas}}, D_{\mathrm{LO,meas}}\right) - \varphi_{m,\mathrm{ref}}\left(D_{\mathrm{sig,ref}}, D_{\mathrm{LO,ref}}\right) \\
&= \left(2z + D_{\mathrm{sig,meas}} - D_{\mathrm{LO,meas}} - \left(D_{\mathrm{sig,ref}} - D_{\mathrm{LO,ref}}\right)\right)m\omega_{\mathrm{mod,sig}}\big/c \\
&\quad + \left(2z + D_{\mathrm{sig,meas}} - D_{\mathrm{LO,meas}} - \left(D_{\mathrm{sig,ref}} - D_{\mathrm{LO,ref}}\right)\right)\omega_{0,\mathrm{sig}}\big/c \\
&\quad - \left(D_{\mathrm{LO,meas}} - D_{\mathrm{LO,ref}}\right)\Delta\omega_0\big/c \\
&\quad - \left(D_{\mathrm{LO,meas}} - D_{\mathrm{LO,ref}}\right)m\Delta\omega_{\mathrm{mod}}\big/c.
\end{aligned}
\tag{13}
$$

Subtracting the values $\Delta\varphi_m(z_0)$ from a calibration measurement at the position z_0, we arrive at Eq. (1),

$$
\delta\varphi_m(z) = \Delta\varphi_m(z) - \Delta\varphi_m(z_0) = 2(z - z_0)m\,\omega_{\mathrm{mod,sig}}\big/c + 2(z - z_0)\,\omega_{0,\mathrm{sig}}\big/c.
\tag{14}
$$

The distance $z - z_0$ can thus be extracted by extracting the slope of the linear relationship between $\delta\varphi_m$ and m.

Appendix B: Optimum power splitting ratio

In the following section we derive an expression for the optimum splitting ratio of the TPS, see Fig. 1(a), used to distribute the power of the LO comb FC 1 to measurement and reference photodetectors. Due to the relatively low optical powers impinging on the detectors, the

current system is limited by thermal noise. The noise current variance is thus independent of the optical power and denoted as $\sigma_{I,\text{noise}}^2$. For simplicity, we assume that both detectors feature the same noise current variance. The optical power of a comb line is given as $P_m = Z_0^{-1} \left\langle E_m^2(t) \right\rangle = Z_0^{-1} \left\langle \hat{E}_m^2 \cos^2(\omega_m t) \right\rangle = \frac{1}{2} Z_0^{-1} \hat{E}_m^2$, where $\left\langle - \right\rangle$ denotes the average over a few carrier periods. Using this relation and Eq. (8) with $m = l$, the power signal-to-noise ratio SNR_m of a single IF line with index m is given by

$$\text{SNR}_m = \frac{\frac{1}{2} S^2 2 P_{m,\text{sig}} 2 P_{m,\text{LO}}}{\sigma_{I,\text{noise}}^2} \tag{15}$$

For distance measurement, we valuate the phase of theses IF lines. The accuracy is thus dictated by the phase variance $\sigma_{\varphi,m}^2$, which is given by [45]

$$\sigma_{\varphi,m}^2 = \frac{1}{2 \times \text{SNR}_m}. \tag{16}$$

The distance z is calculated from a linear regression of the phase differences $\Delta\varphi_m = \varphi_{m,\text{meas}} - \varphi_{m,\text{ref}}$ between measurement and reference detector. For simplification, we assume a number of N spectrally uniform IF lines with equal SNR and drop the index m. The noise of measurement and reference detector is statistically independent such that the phase variances can be added,

$$\sigma_{\Delta\varphi}^2 = \sigma_{\varphi,\text{meas}}^2 + \sigma_{\varphi,\text{ref}}^2. \tag{17}$$

Then the variance of the measured distance z is given from the analytic formula for the slope uncertainty of a linear regression [46] and is proportional to the variance of the phase difference $\sigma_{\Delta\varphi}^2$,

$$\sigma_z^2 = \frac{\sigma_{\Delta\varphi}^2}{N} \frac{3}{\left(\omega_{\text{mod,sig}}/c\right)^2 \left(N^2 - 1\right)}. \tag{18}$$

With Eq. (15) and Eq. (16), Eq. (17) can be written as

$$\sigma_{\Delta\varphi}^2 = \frac{\sigma_{I,\text{noise}}^2}{4 S^2} \left(\frac{1}{P_{\text{sig,meas}} P_{\text{LO,meas}}} + \frac{1}{P_{\text{sig,ref}} P_{\text{LO,ref}}} \right) \tag{19}$$

We consider Fig. 6 to express the optical powers of the comb lines impinging on the respective detectors in Eq. (19) in the following way: The input power into the TPS is denoted as P_{LO}. With the power splitting ratio γ, $P_{\text{LO,meas}} = (1-\gamma) P_{\text{LO}}$ and $P_{\text{LO,ref}} = \gamma P_{\text{LO}}$. The additional power loss of $P_{\text{sig,meas}}$ compared to $P_{\text{sig,ref}}$ is denoted η, $\eta = P_{\text{sig,meas}}/P_{\text{sig,ref}}$, as discussed in Section 3. With these relations, we can write Eq. (19) as

$$\sigma_{\Delta\varphi}^2 = \frac{\sigma_{I,\text{noise}}^2}{4 S^2 P_{\text{LO}} P_{\text{sig,ref}}} \left(\frac{1}{\eta(1-\gamma)} + \frac{1}{\gamma} \right). \tag{20}$$
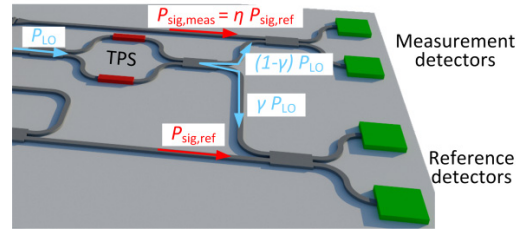
Fig. 6. Schematic of power distribution on measurement and reference detectors. $P_{\text{sig,meas}}$ is subject to an additional measurement path loss of $\eta_{\text{dB}} = 10 \lg(\eta) = -23\,\text{dB}$ when compared to $P_{\text{sig,ref}}$ due to coupling losses, see Fig. 1 and the discussion in Section 3. The power of the LO comb FC 1 is distributed between both detectors by the TPS with a tunable power splitting ratio of γ.

The power splitting ratio γ can easily be adapted by changing the interference conditions of the MZM forming the TPS. For a maximum measurement precision, the goal is to minimize $\sigma^2_{\Delta\varphi}(\gamma) \propto \sigma^2_z$, Eq. (20). We find a minimum at

$$\gamma_{\min} = \frac{1}{1 + \eta^{-1/2}} \tag{21}$$

In our case $\eta_{\text{dB}} = 10 \lg(\eta) = -23\,\text{dB}$. Inserting this value in Eq. (21), we calculate a theoretical optimum value of $\gamma_{\min,\text{dB,theo}} = 10 \lg(\gamma_{\min}) = -11.8\,\text{dB}$. This is close to the experimentally measured value of $\gamma_{\min,\text{dB}} = -10.2\,\text{dB}$.